Measurements of sound propagation in Mars' lower atmosphere

Baptiste Chide [a,*], Xavier Jacob [b], Andi Petculescu [c], Ralph D. Lorenz [d], Sylvestre Maurice [e], Fabian Seel [f], Susanne Schröder [f], Roger C. Wiens [g], Martin Gillier [h], Naomi Murdoch [h], Nina L. Lanza [a], Tanguy Bertrand [i], Timothy G. Leighton [j], Phillip Joseph [j], Paolo Pilleri [e], David Mimoun [h], Alexander Stott [h], Manuel de la Torre Juarez [k], Ricardo Hueso [l], Asier Munguira [l], Agustin Sánchez-Lavega [l], German Martinez [m,n], Carène Larmat [a], Jérémie Lasue [e], Claire Newman [o], Jorge Pla-Garcia [p], Pernelle Bernardi [i], Ari-Matti Harri [q], Maria Genzer [q], Alain Lepinette [p]

[a] Space and Planetary Exploration Team, Los Alamos National Laboratory, Los Alamos, NM, USA
[b] Institut de Mécanique des Fluides de Toulouse, Université de Toulouse III Paul Sabatier, INP, CNRS, Toulouse, France
[c] Department of Physics, University of Louisiana at Lafayette, Lafayette, LA, USA
[d] Space Exploration Sector, Johns Hopkins Applied Physics Laboratory, Laurel, MD, USA
[e] Institut de Recherches en Astrophysique et Planétologie (IRAP), Toulouse, France
[f] Institute of Optical Sensor Systems, German Aerospace Center (DLR), Berlin, Germany
[g] Department of Earth, Atmospheric, and Planetary Sciences, Purdue University, West Lafayette, IN, USA
[h] Institut Supérieur de l'Aéronautique et de l'Espace (ISAE-SUPAERO), Université de Toulouse, Toulouse, France
[i] LESIA, Observatoire de Paris, Université PSL, Sorbonne Université, Université de Paris, CNRS, Meudon, France
[j] Institute of Sound and Vibration Research, University of Southampton, Southampton, United Kingdom
[k] Jet Propulsion Laboratory, California Institute of Technology, Pasadena, CA, USA
[l] Física Aplicada, Escuela de Ingeniería de Bilbao, UPV/EHU, Bilbao, Spain
[m] Lunar and Planetary Institute, Universities Space Research Association, Houston, TX, USA
[n] Department of Climate and Space Sciences and Engineering, University of Michigan, Ann Arbor, MI, USA
[o] Aeolis Research, Chandler, AZ, USA
[p] Centro de Astrobiología (INTA-CSIC), Madrid, Spain
[q] Finnish Meteorological Institute, Helsinki, Finland

ARTICLE INFO

ABSTRACT

Acoustics has become extraterrestrial and Mars provides a new natural laboratory for testing sound propagation models compared to those ones on Earth. Owing to the unique combination of a microphone and two sound sources, the Ingenuity helicopter and the SuperCam laser-induced sparks, the Mars 2020 Perseverance rover payload enables the *in situ* characterization of unique sound propagation properties of the low-pressure CO_2-dominated Mars atmosphere. In this study, we show that atmospheric turbulence is responsible for a large variability in the sound amplitudes from laser-induced sparks. This variability follows the diurnal pattern of turbulence. In addition, acoustic measurements acquired over one Martian year reveal a variation of the sound intensity by a factor of 1.8 from a constant source due to the seasonal cycle of pressure and temperature that significantly modifies the acoustic impedance and shock-wave formation. Finally, we show that the evolution of the Ingenuity tones and laser spark amplitudes with distance is consistent with one of the existing sound absorption models, which is a key parameter for numerical simulations applied to geophysical experiments on CO_2-rich atmospheres. Overall, these results demonstrate the potential of sound propagation to interrogate the Mars environment and will therefore help in the design of future acoustic-based experiments for Mars or other planetary atmospheres such as Venus and Titan.

1. Introduction

Outdoor sound propagation undergoes numerous and complex interactions with the atmosphere through which it travels, as it

is driven by thermodynamics and meteorological conditions. On Earth this has been extensively studied by theoretical, computational, and experimental works (Attenborough, 2002 for a review), in order to predict sound pressure level of noise and to perform *in situ* sensing of the atmosphere itself. The CO_2-dominated low-pressure atmosphere of Mars provides us with a whole new set of atmospheric properties and dynamic conditions, which significantly affect the propagation of sounds compared to Earth.

To explore how atmospheric properties affect sound propagation in the Martian atmosphere, we examine two acoustic experiments conducted on the surface of Mars by NASA's Perseverance rover. The sound source is either a shock wave or a mechanical sound, both at various distances. The receiver is a microphone installed on the SuperCam instrument in the upper part of the Remote Sensing Mast of the rover. In these experiments, which involve the propagation of spherical waves, the sound pressure p at a distance r from a source is given by:

$$p(r) = p^* r^* \times \beta_{src} \times H_c \times \frac{e^{-\alpha(r-r^*)}}{r} \tag{1}$$

where p^* is the acoustic pressure measured at a reference distance r^*; β_{src} represents the variations of the source intensity; H_c accounts for the coupling between the source and the atmosphere on one hand, and between the atmosphere and the recording device on the other hand. This coupling, representing the budget of acoustic energy transferred through the different interfaces, is controlled by the acoustic impedance of the atmosphere, Z_{ac}, which mostly depends on the atmospheric density. In a planetary atmosphere, density is directly related to temperature T_0 and pressure P_0. On Mars, the surface pressure experiences a large seasonal cycle due to the condensation and sublimation of carbon dioxide at the polar caps, with average daily values at Jezero crater ranging from 625 Pa to 800 Pa between Northern summer and winter (Sanchez-Lavega et al., 2023). The temperature itself ranges from 195 K to 260 K at 1.5 m above the surface, modulated on the long-term by the seasonal cycle and thermal tides and on the short term by different dynamical phenomena (Martinez et al., 2023; Munguira et al., 2023). Low pressure and cold temperature relative to Earth (the density is less than 1% of that measured on Earth) lead to an overall poor and variable coupling efficiency for acoustic waves. The sound amplitude is also attenuated along its propagation path because of the geometric spreading of the wavefront (as the inverse of the distance) and because of energy exchanges with molecules of the atmosphere. The latter effect is modeled by the attenuation coefficient, α. It mostly depends on the atmospheric composition and it is a function of the frequency of the wave. For a low-pressure, CO_2-rich atmosphere such as on Mars, physical models of sound propagation predict an attenuation ten times higher than on Earth (Williams, 2001; Bass and Chambers, 2001; Petculescu and Lueptow, 2007). Moreover, Mars' Planetary Boundary Layer (PBL, which corresponds to the lowest layer of the atmosphere in direct contact with the surface) is also prone to an intense convective turbulence during the daytime (Petrosyan et al. (2011) for a general review and for direct evidence in Jezero crater see Munguira et al. (2023); De la Torre-Juarez et al. (2023)), which is initiated by the strong thermal gradient between the surface and the atmosphere right above. These turbulent small scale eddies induce a random scattering of acoustic waves (Blanc-Benon and Juve, 1993). The NASA Perseverance rover carries the first sensors able to confirm these theoretical predictions of sound propagation on Mars.

In 2021, Perseverance landed at Jezero crater (Northern hemisphere, 18.4°N, 77.5°E), Mars, with a unique combination of a scientific microphone and two sound sources at various distances and distinct in frequency. The SuperCam microphone (Maurice et al.,

2021; Mimoun et al., 2023) records the Mars soundscape between 20 Hz and 50 kHz, as well as artificial sounds produced by Perseverance and Ingenuity activities (Maurice et al., 2022). In particular, it is able to record the high frequency (2 kHz–25 kHz) acoustic signal generated by the SuperCam laser vaporizing nanogram quantities of rocks per laser pulse at their surface (Chide et al., 2022) and the low frequency tones (84 and 168 Hz) of the Ingenuity rotorcraft flights (Lorenz et al., 2023). Therefore, this emission-reception experiment turns Jezero crater into an open-air laboratory to test our theoretical understanding of how different sound propagation is on Mars with respect to Earth.

In this study, we analyze the laser-induced acoustic amplitudes recorded over the first Martian Year of Perseverance's mission, Martian Year 36, from the landing at $L_s = 5.1°$, up to $L_s = 360°$, where L_s is the areocentric solar longitude. This period corresponds to the first 657 Sols of the mission (a Sol is a Martian solar day; landing was on Sol 0). We also use three Ingenuity flights recorded early in the mission ($L_s = 38$–$49°$) and we compare these data with the atmospheric pressure and temperature (see Supplementary Material Text S1 for data set) retrieved by the Mars Environmental Dynamics Analyzer, MEDA (Rodriguez-Manfredi et al., 2021). These two sound sources are characterized in distance and frequency (Section 2). Recording of these sounds with the SuperCam microphone and the study of their respective amplitudes with distance, local time and seasons, enables the *in situ* measurement of the Mars sound propagation properties highlighted above: the scattering by turbulence (Section 3.1), the seasonal variation of the acoustic impedance (Section 3.2), and the absorption with frequency (Section 3.3).

2. Sound sources on Mars

2.1. Laser-induced acoustic signal

The Laser-Induced Breakdown Spectroscopy (LIBS) capability of the SuperCam instrument suite (Wiens et al., 2020; Maurice et al., 2021) is used to study the chemistry of Mars' surface by analyzing the optical emission lines radiating from a plasma plume, which is excited by a laser pulse focused on a solid target at distances of up to several meters. The expansion of the hot laser-induced plasma in Mars' rarified atmosphere generates a blast wave and leads to a distinct acoustic signal, which is recorded by the SuperCam microphone to complement LIBS investigations (Murdoch et al., 2019, Chide et al., 2019, 2021; Seel et al., 2023). A typical LIBS experiment to analyze a target consists of several separate bursts of 30 to 150 laser pulses (shots), which are fired at a cadence of 3 Hz. The microphone records the entire burst with the exception of the last shot. For each target, 5 to 10 bursts are repeated on points arranged in a certain raster and separated by a few millimeters. An autofocus procedure is performed on some points of the raster, in order to maximize the laser irradiance deposited on the target's surface and from which the instrument-to-target distance is precisely obtained. As the focal distance increases, the focused laser beam radius increases, which reduces the irradiance (in W/cm^2) deposited on the target surface with the distance (Maurice et al., 2021). Consequently, the ablation is less efficient and the blast wave is weaker for increasing distances. The irradiance I, as a function of the distance of the target, r, was measured before launch and can be fitted as (see Supplementary Material Figure S2):

$$I(r) = I_0 e^{-(0.53\pm0.03)r} \tag{2}$$

Targets are located at distances from 1.98 m to 8.80 m and shots are performed during the daytime on Mars, between 7:06

and 19:01 Local True Solar Time (LTST). The first joint LIBS-microphone analysis occurred at $L_s = 22°$ (Sol 37). Each laser-induced acoustic wave is recorded over a 60 ms time-window triggered on the laser ignition, at a sampling frequency of 100 kHz to avoid any aliasing from electromagnetic perturbations. This time window records the direct arrival of the acoustic wave but also the echoes from reflection of the structure of the instrument and on nearby rocks. In order to minimize the influence of these echoes on the time series and on the associated frequency spectrum, the direct wave is identified and then fitted with a theoretical Gaussian pulse (Taylor 1950; see Supplementary Material Text S2 and Figure S1). For each shot, the peak amplitude of the fitted compression wave is extracted and considered as the 'bulk' metric for the evolution of the laser-induced acoustic signal. Moreover, laboratory studies have shown that the laser-induced acoustic signal amplitude is proportional to the square root of the laser irradiance deposited on the target (Chide et al., 2020). Therefore, the sound propagation applied to LIBS sparks becomes:

$$p_{LIBS}(r) = p^* r^* \times \sqrt{I(r)} \times \frac{e^{-\alpha(r-r^*)}}{r} * H_c(P_0, T_0)$$

$$p_{LIBS}(r) \propto \frac{1}{r} e^{-\left(\alpha + \frac{0.53}{2}\right)r} * H_c(P_0, T_0) \tag{3}$$

2.2. Ingenuity flights

The Ingenuity helicopter (Balaram et al., 2021), released by Perseverance shortly after landing performed the first autonomous rotorcraft flight on another planet. Since then it has flown 37 times (up to Sol 657) as close as 50 m from the rover. Four flights (#4, #5, #6 and #8) were close enough, <150 m, for their acoustic signatures to be recorded by the SuperCam microphone (Lorenz et al., 2023). They consist of tones at 84 Hz (at the blade crossing frequency, i.e., 2537 rpm, Grip et al. (2022)) and its first harmonic at 168 Hz for the closest distances, <90 m. Higher harmonics were not detected, likely because of the larger absorption for higher frequencies. Given the small size of the source compared to the propagation distance, these acoustic radiations are considered to be spherical waves. For each flight, the tones at 84 Hz and 168 Hz were fitted with a Gaussian function (see Supporting Figure S2) and their magnitudes were compared to the microphone-to-helicopter distance, extracted from the flight trajectories presented in Lorenz et al. (2023). In the data of flight #8, the 84 Hz tone is mostly masked by the wind noise, and the data were, therefore, excluded. The flights that are considered were performed between $L_s = 38°$ to $49°$, all around noon local time. Therefore, it is considered that atmospheric conditions, e.g. pressure, temperature, winds (Lemmon et al., 2022), and, therefore, the source-to-atmosphere coupling (see Section 3.2), remained roughly the same for flights #4, #5 and #6. Furthermore, the experimental parameters of the flights that could affect the sound (e.g. rotor speed, translation speed) did not vary between these flights. Consequently, the sound propagation with distance, Equation (1), applied to Ingenuity tones p_{tones}, becomes:

$$p_{tones} = p^* r^* \times \frac{e^{-\alpha(r-r^*)}}{r} \tag{4a}$$

This is equivalent to:

$$\ln(p_{tones} \times r) = K - \alpha r, \tag{4b}$$

with K being a constant independent from the distance.

3. Results

3.1. Turbulence-induced scattering of amplitudes

For a sequence of consecutive laser shots on a target, a scattering of the laser-induced acoustic signal amplitude is observed on the time series (Fig. 1a) and on the associated peak amplitude distribution (Fig. 1b). It varies with the local time of the acquisition and the distance to the target: the dispersion is small at dusk (target AEGIS_461A) with amplitudes within ±4% (standard deviation) around the median value and a dispersion that is symmetric around the median. For the same distance, the scatter increases for an acquisition around noon (target Ubraye, ±10%) when the atmospheric turbulence is typically close to its maximum. For the same local time but for longer distance the scatter increases drastically (target Bezaudun, ±18%) with the appearance of some high-amplitude peaks, which are amplified more than twice the median amplitude. This could potentially be due to caustics that randomly focus the acoustic wave (Blanc-Benon et al., 1991) towards the microphone. Therefore, as the tail lengthens towards the high amplitudes, the distribution becomes asymmetric and is centered towards the left of the median. This behavior is consistent with observations of N-waves propagating through turbulence (e.g., Salze et al. (2014) for short wavelength pulses propagating through controlled thermal turbulence and Arrowsmith et al. (2022) for infrasonic blasts). The distribution of peak amplitudes, $W(P)$, can be fitted with a gamma distribution (Averiyanov et al., 2011; Salze et al., 2014):

$$W(P) = \frac{P^{a-1} e^{-\frac{P}{b}}}{b^a \Gamma(a)} \tag{5}$$

with P being the normalized peak amplitude, Γ the gamma function and a, b two fitted parameters. The agreement between the distribution and the fit is excellent for the Mars targets. However, one known source of shot-to-shot variation is the contribution from the hardness of the target, which results in a monotonic decrease in shot-to-shot amplitude (Chide et al., 2019; Murdoch et al., 2019). It was reported that the decrease could be as high as 30% over 30 shots for the softest targets and it would deviate from a gamma distribution. Hence, given the shape of the distribution and the magnitude of the amplitude scattering, we assume that only the turbulence can explain the scattering observed in the Mars data.

For the targets acquired at dusk or dawn (e.g. target AEGIS_461A), $a \gg 1$. Hence, the gamma distribution converges to a log-normal distribution, which corresponds to a weak thermal fluctuation regime of the atmosphere (Blanc-Benon and Juve, 1993). This is consistent for dusk and dawn on Mars, when atmospheric turbulence has barely initiated yet or has vanished, respectively. For the daytime observations, the distribution never converges toward an exponential distribution (where a would be expected to tend to 1), meaning that the atmosphere stays in an intermediate fluctuation regime and never reaches the strong fluctuations regime (Blanc-Benon and Juve, 1993). The fitted distributions also confirm the shift of the center toward the left of the median as the distance increases, which supports the hypothesis of the formation of caustics.

The two parameters retrieved from the fit of the distributions with Equation (4b) are then used to compute the statistical mode P_{mode} (i.e., the most frequent value of the amplitude distribution) and the standard deviation of the distribution, σ_P, for each target (Thom, 1958):

$$P_{mode} = (a-1)b \tag{6}$$

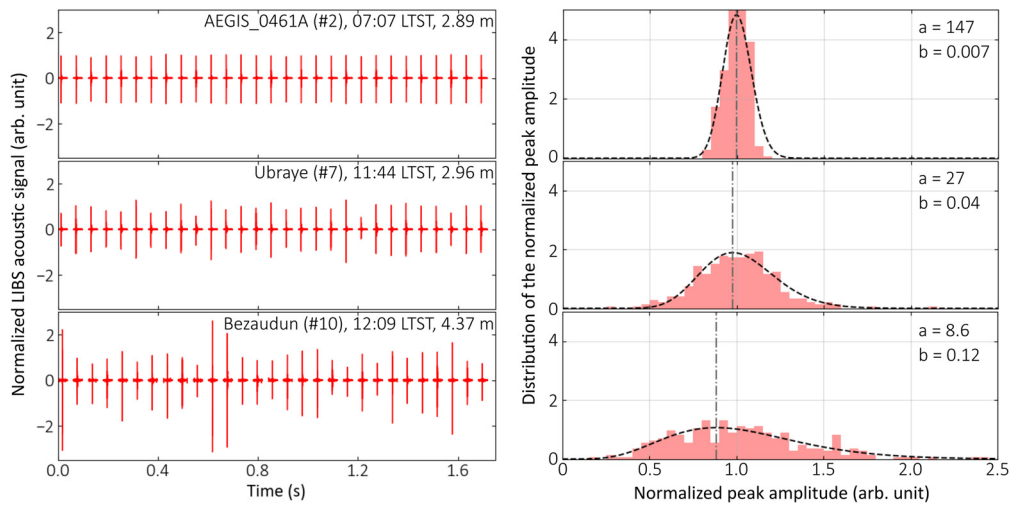$$\sigma_P = \sqrt{ab^2} \tag{7}$$

Fig. 1. Evolution of the laser-induced acoustic signal acquired for three targets at different local times and distance (a) Bursts of 29 shots showing the shot-to-shot variation of the signal amplitude. The time series are normalized by the median of the peak amplitude over the 29 shots. (b) Distributions of the normalized peak amplitude for the three targets (each histogram is computed using combined data from 5 consecutive raster bursts, i.e. 195 shots, see Supporting Information Text S3). Distributions are fitted with a gamma distribution (dashed black, see Equation (4b)), whose parameters are listed on the top right corner of each panel.

As inferred previously, Fig. 2a confirms that the mode of the amplitude distribution decreases relative to the median for increasing distance, due to caustics that overestimate the median of the distribution. Therefore, and in the following, the representative metric considered for the absolute acoustic amplitude over a burst will be the mode of the distribution rather than the median over a target.

One also notices in Fig. 1b that the amplitude scattering σ_P also increases for targets that are more distant; this evolution is presented in Supplementary Material Figure S4. As expected σ_P follows a power law as a function of the distance, as predicted on Earth with experiments and theoretical predictions for spherical waves (Blanc-Benon and Juve, 1993). The examination of the details of this relationship is beyond the scope of this study and upcoming investigations will focus on the analytical equations linking the sound amplitude scattering with the propagation parameters such as the distance and the turbulence length scale of the Mars atmosphere. However, this relationship presented in Supporting Figure S3 is used to normalize σ_P with respect to the distance, by dividing σ_P by $(r/r_0)^{0.64}$ (with $r_0 = 2$ m). Then, this normalization reveals the evolution of σ_P as a function of the local time (Fig. 2b). It is compared with the daytime evolution of the temperature fluctuations retrieved from MEDA (Munguira et al., 2023), which is indicative of convective instabilities. The daytime pattern of the amplitude scattering matches the daytime evolution of the temperature fluctuations, with an increase of the scattering during the morning to reach a maximum around 13:00 LTST, then a decrease until late afternoon when the boundary layer collapses. The amplitude of the dispersion of the acoustic signal is wider than that of the temperature fluctuations, with notably points of low dispersion at noon. However, the acoustic scattering is computed over a 10-second long sequence of laser shots whereas the MEDA temperature fluctuation is computed over a 5-minute long window. Indeed, Stott et al. (2023) have pointed out that in during 2-minute long sound recordings, there can be quiet periods over a 10-second timescale, even though the average turbulence over the entire recording is strong. The scattering of amplitudes in Fig. 2b also matches the sound speed-derived temperature fluctuations observed with the microphone (Chide et al., 2022), which was already shown to be a new indicator of rapid air temperature fluctuations on Mars. Therefore, we confirm that acoustic signal scattering is consistent with the daytime development of the turbulence near the surface. Lastly, Fig. 2b shows an increasing trend

of the scattering after 18:00 LTST. As discussed in Chide et al. (2022), some of these points are due to an enhanced turbulence caused by the warm plumes brought from the rover's radioisotope thermal generator. It could also highlight some amplitude variations due to the rock itself.

Overall, the turbulence on Mars induces random fluctuations on the laser-induced acoustic signals, which might lead to the obscuring of some small shot-to-shot variations of amplitude needed to constrain rock hardness or surface coatings on Mars (Chide et al., 2020; Lanza et al., 2020). Therefore, for such purposes, observations acquired at short distance and in low turbulence conditions (dusk or dawn, after 17:00 LTST) should be given priority. As the shot-to-shot scattering of the acoustic amplitude for each target is now characterized and quantified, this allows to conduct, in the next section, the target-to-target comparison of the absolute acoustic amplitudes.

3.2. Acoustic impedance and atmospheric coupling

For the first time, owing to the survey over one Martian year of the laser-induced acoustic signal amplitude, we measure seasonal variations of the acoustic impedance on Mars and understand how to correct SuperCam recordings accordingly. The laser-induced acoustic signals acquired over nearly a Martian year respond to seasonal changes at the plasma-atmosphere and microphone-atmosphere interfaces, which are caused by the temperature and pressure cycles of the Mars atmosphere. In this section, for each acoustic point, we consider the mode of the distribution described in Section 3.1 as the recorded laser-induced acoustic amplitude. Then, in order to compare recordings acquired at various distances, sound amplitudes are corrected for the atmospheric and instrumental attenuation: the decrease of the sound amplitude as a function of the distance is fitted following Equation (2) and subsequently normalized to 2 m, the distance of the closest target of the dataset.

Fig. 3a plots the distance-normalized acoustic amplitudes as a function of the solar longitude, L_s. It is compared to the seasonal changes of pressure and to the air temperature at 12:00 LTST computed from MEDA data (Fig. 3b and c). The gap in the acoustic data coverage between $L_s = 180$ to $215°$ is due to a rapid traverse of the rover from the crater floor to the delta front during which no SuperCam laser activity was allowed. Although the number of targets sampled decreases when the rover has reached the delta, it
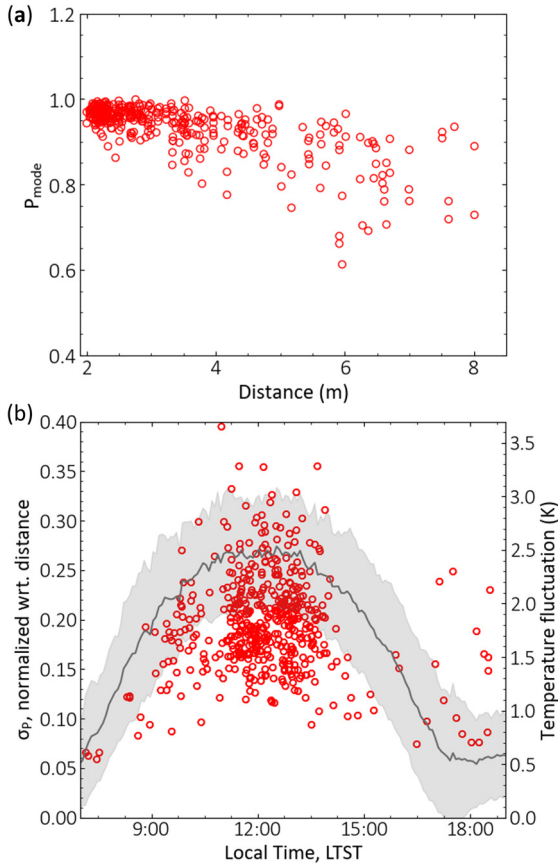
Fig. 2. (a) Evolution of the mode of the amplitude distribution relative to the median, P_{mode} (see Equation (5)) as a function of the microphone-to-target distance. (b) Standard deviation of the amplitude relative to the median for each target, σ_P (see Equation (6)), as a function of the local time of the acquisition (red points). σ_P is normalized to the distance of the target (see Supporting Figure S3). It is compared with the temperature fluctuations in 5-minute long windows over the first 400 Sols from the MEDA temperature sensors at 1.45 m (data from Munguira et al. (2023)): mean of the fluctuations: solid line, standard deviation of the fluctuations: shaded area. For both panels, values are normalized by the median peak amplitude over a target.

is noticed that the scattering of the data points after $L_s = 215°$ tends to be higher than during the first part of the year. Even with this spread of the amplitudes, which is mostly associated with the turbulence-induced scattering, a clear seasonal trend is observed: the average sound amplitude decreases from $L_s = 50°$ down to $L_s = 160°$ (close to the autumn equinox, $L_s = 180°$) to reach an average minimum value of 0.25 Pa. Then it increases to an average maximum value of 0.45 Pa at $L_s = 270°$ for winter solstice. Overall, the average peak sound amplitude varies by a factor 1.8 over a Martian year. This annual cycle follows the annual cycle of pressure and temperature variations: the sound amplitude decreases during Northern spring and summer when air density decreases (i.e. pressure decrease and warmer air temperatures). Inversely, the sound amplitude increase is consistent with a sharp pressure increase and an air-cooling during fall ($L_s = 180-270°$).

These seasonal variations of the sound amplitude are the result of the combination of two effects: (1) a modification of the shock wave pressure at the source of the acoustic signal, and (2) a variation of the coupling between the atmosphere and the microphone membrane at the end of the propagation path, i.e., a variation of the acoustic impedance. The seasonal effects on the shock wave can be modeled by using the Rankine-Hugoniot conditions that describe how the shock wave pressure, p_{sw} (Zel'dovich

and Raizer, 1967) is related to the shock-front speed, D, and other atmospheric quantities:

$$p_{sw} = \frac{2}{\gamma + 1} \rho_0 D^2 \tag{8}$$

with, ρ_0 the atmosphere density and γ the adiabatic ratio. The laser-induced shock-wave radius $R(t)$ expands as a function of time, t, following the strong point explosion model (Taylor, 1950; Campanella et al., 2019; Seel et al., 2023):

$$R(t) = \xi \left(\frac{E}{\rho_0} \right)^{\frac{1}{5}} t^{\frac{2}{5}} \tag{9}$$

where ξ is a constant and E the energy released in the shock. Therefore, the speed of the shock front can be expressed as:

$$D = \frac{dR}{dt} = \frac{2}{5} \xi \left(\frac{E}{\rho_0} \right)^{\frac{1}{5}} t^{\frac{-3}{5}} \tag{10}$$

Combining Equations (6) and (10) shows that the shock-front pressure is a function of the atmospheric density:

$$p_{sw} = \frac{2}{\gamma + 1} \left(\frac{2}{5} \xi \right)^2 \left(\frac{E^2}{t^6} \right)^{\frac{1}{5}} \rho_0^{3/5} \propto \rho_0^{3/5} \tag{11}$$

The Mars atmosphere is considered as an ideal gas whose ambient density is $\rho_0 = \frac{P_0 M}{\mathcal{R} T_0}$, with M the molar mass of the atmosphere, $\mathcal{R}$ the ideal gas constant (8.314 J.K^{-1}.mol^{-1}), P_0 and T_0 the background pressure and temperature, respectively. Thus, the dependence of the shockwave amplitude on the ambient specifications becomes:

$$p_{sw} \propto \left(\frac{P_0 M}{T_0} \right)^{3/5} \tag{12}$$

At the other end of the propagation path, the amount of acoustic energy that is coupled across the atmosphere-microphone interface is a function of the characteristic acoustic impedance of the atmosphere, $Z_{ac} = p/u$, with p the sound pressure and u the particle velocity (Dalmont, 2001). With the assumption that the particle velocity is the same for all laser sparks and that there is no phase shift between p and u, the sound pressure recorded by the microphone becomes proportional to the impedance. The characteristic acoustic impedance, which basically describes the ability of the atmosphere to couple with the microphone membrane, is defined as:

$$Z_{ac} = \rho_0 c \tag{13}$$

with c being the speed of sound. Still considering an ideal gas law where $c^2 = \frac{\gamma \mathcal{R} T_0}{M}$, the acoustic impedance is written as:

$$Z_{ac} = \sqrt{\frac{\gamma M}{\mathcal{R}}} P_0 T_0^{-1/2} \tag{14}$$

Combining Equations (10) and (12), the sound pressure recorded by the microphone varies with ambient the pressure and temperature according to:

$$p_{recorded} \propto p_{sw} Z_{ac} \propto P_0^{8/5} T_0^{-11/10} \tag{15}$$

Based on this theory, sound amplitude data in Figs. 3a and d are compared with the ratio $P^{8/5}/T^{11/10}$. This comparison demonstrates that the correlation between sound amplitude and $P^{8/5}/T^{11/10}$ is verified, which confirms the atmospheric origin of the seasonal amplitude variation recorded in the acoustic data. As
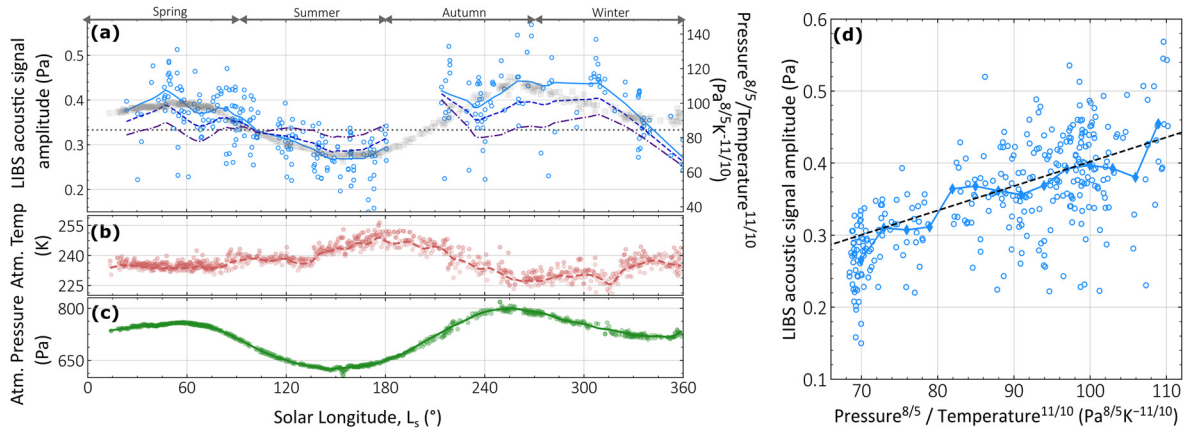
Fig. 3. (a) Seasonal evolution of the LIBS acoustic signal amplitude between 11:00 and 14:00 LTST (blue points). All amplitudes are normalized to a distance of 2 m. The solid light blue line represents a smoothing over 30° of solar longitude. This smoothed trend is subsequently corrected for the Rankine-Hugoniot shock condition (dark blue, dashed) and for the acoustic impedance variation (purple, dashed-dotted) – see text. Both corrections are normalized to a temperature of 240 K and a pressure of 700 Pa (i.e., atmospheric conditions at $L_s = 90°$). The data are superimposed with the seasonal variation of the ratio $P^{8/5}/T^{11/10}$ (gray squares), which comes from the theory described in Equation (13) and is computed from the data in panels b and c. The dotted horizontal line corresponds to the median corrected amplitude. (b) Seasonal evolution of air temperature at a height of 1.5 m at 12:00 LTST. (c) Seasonal evolution of atmospheric pressure at 12:00 LTST. (d) Correlation between the LIBS acoustic signal amplitude normalized to a distance of 2 m and $P^{8/5}/T^{11/10}$ computed with the MEDA data for each acoustic point. Circles represent all the data points whereas diamonds represent a running mean subset.

expected, the seasonal sound evolution is dominated by the pressure cycle. Therefore, the amplitudes in Fig. 3a are subsequently corrected for the acoustic impedance variation (dark blue dashed line) and from the modification of the shock pressure (purple dashed-dotted line). This correction removes the seasonal trend of the sound amplitude caused by atmospheric variations: the corrected line is flatter compared to the uncorrected line. Especially, during the first half of the year, up to $L_s = 180°$, the corrected amplitudes experience some small variations, within ± 8% around the median.

Still, the corrected data exhibit some larger deviations: between $L_s = 280$ to $330°$ (Sols 512–600) the corrected amplitude is higher than its median with a maximum value up to +11% (peak at $L_s = 310°$; Sol 568). Then after $L_s = 330°$, the corrected amplitude is lower than the median and goes down to −23% of the median at $L_s = 360°$ (Sol 657). The effect of the molar weight is ruled out as it varies by less than 0.5% over a Martian year (Trainer et al., 2019). However, as noticed earlier, we observe a larger scattering of our data in the second half of the year after $L_s = 210°$, after the rover's arrival at the delta front. This enhanced scattering might be due to change in topography that could influence the local atmospheric dynamic or seasonal effect with an increased turbulence during the Northern autumn and winter as already observed with In-Sight (Chatain et al., 2021). This larger scattering is also associated with a reduced number of samples during this period. Considering these two factors, the running averages in Fig. 3a have larger uncertainties and it could explain these larger deviations. These two deviations from the median are also concomitant with the rover's exploration of different strata of the delta front with sedimentary rocks significantly different in texture, composition and mineralogy from the two igneous units visited before. Consequently, this change in rock parameters might affect the laser-matter interaction that controls the amount of energy released in the shock wave. However, the relationship between target properties and the laser-matter coupling is still poorly understood (Chide et al., 2020). Therefore, this hypothesis should be investigated further and compared with the elemental composition retrieved with LIBS for each target. To that end, the atmospheric correction proposed here is a prerequisite and a critical step. This correction is also necessary to study the sound amplitude evolution as a function of the distance for the entire dataset and, therefore, to retrieve the acoustic absorption.

3.3. Acoustic absorption

One particularly interesting aspect of the two artificial sound sources, the laser sparks and the helicopter, is that they are recorded at varying distances from the microphone, from 2 to 8 m and from 70 to ~150 m respectively. Hence, these experiments enable the computation of the relative sound absorption with distance, and therefore, the retrieval of the attenuation coefficient, α. This is done in two distinct frequency bands: at high frequency with the laser sparks, in a range where the viscosity and thermal absorption dominate, and at low frequency for the helicopter, where vibrational relaxation prevails and where models are less constrained for Mars.

For the laser-induced acoustic signals, the frequency spectra of the fitted acoustic pulse (see Supplementary Material Text S1) are integrated over ten frequency bands, centered from 3 kHz to 21 kHz, each spaced by 2 kHz and each been 2 kHz large. Subsequently, the amplitude over each band is corrected for the turbulence scattering using the mode of the distribution of the amplitudes for each burst, see Section 3.1, and for atmospheric variation by normalizing with pressure and temperature according to Equation (13) in Section 3.2. For each band, the trend is fitted with Equation (3) to retrieve the attenuation coefficient (Fig. 4b).

For the Ingenuity flights, the amplitudes of the 84 Hz and the 168 Hz tones are extracted when detectable (see Section 2.2). The evolution of the tone amplitudes along flight #4 is given as an example in Fig. 4c. Both the 84 Hz and the 168 Hz show a modulation of their amplitude as a function of the time. This is interpreted as a rotation speed shift between the two blades of about ~50 mHz (confirmed by nadir images taken by the helicopter during the flight). It leads to two blade passage frequencies, slightly different, interfering with each other, which creates destructive gaps modulated by a $\cos^2$ function (Lorenz et al., 2023). Only the maxima of these lobes and their associated distances are considered to compute the attenuation. The evolution of each tone amplitude as a function of the distance is displayed on Fig. 4d. They are fitted with Equation (4b); the attenuation coefficient is given as the slope of the fitted line.

The retrieved attenuation coefficients are displayed in Fig. 5 and compared with the semi-empirical model detailed in Bass and Chambers (2001). Overall, there is an excellent match between the *in situ* data and the model: within the error bars, all points
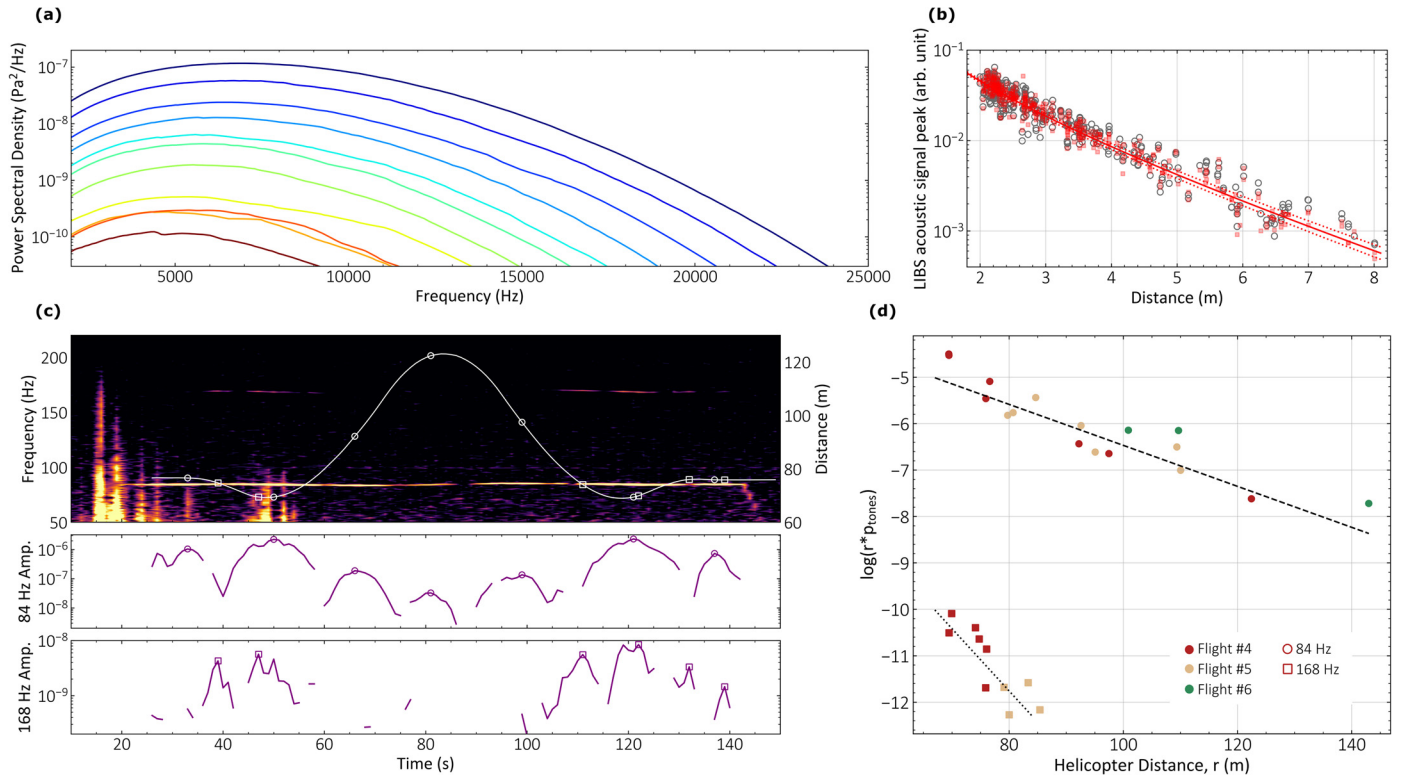
Fig. 4. Computation of the sound amplitude evolution with distance for LIBS sparks and Ingenuity. (a) Power Spectral Density of fitted laser-induced acoustic signal at increasing distances (from dark blue at 2.25 m to dark red at 7.75 m). Each spectrum is computed as the mean spectrum acquired over an interval of 0.5 m. (b) Evolution of the amplitude over the 8 to 10 kHz frequency domain as a function of the distance (raw data: gray circles, turbulence and seasonal cycle corrected: red squares). The corrected data are fitted with Equation (3), red solid. The two red dotted lines indicate the 95% confidence interval of the fit. The uncertainty on the attenuation coefficient is computed by using this interval (c) Upper panel: time-frequency representation of the acoustic signal recorded during Ingenuity flight #3, compared with the helicopter-to-microphone distance along the flight on the secondary y-axis (white markers). Lower panels: evolutions of the 84 Hz and 168 Hz tones along the flight. The markers represent the amplitude of the maximum for each lobe, p_{tones}. The distance, r, at which they were recorded is reported on the upper panel (circles: 84 Hz, squares: 168 Hz). (d) $log(r \times p_{tones})$ as a function of the helicopter distance for each tone and each flight. The fit with Equation (4b) is displayed for each tone (dashed and dotted black lines for the 84 Hz and 168 Hz tones, respectively).

agree with the model. Ingenuity point error bars might be dominated by the turbulence that scatters the tone's amplitude along the ~100 m propagation path whereas laser sparks error bars are mostly due to the uncertainty on the laser irradiance profile. The attenuation points from laser sparks computed here are lower than the one computed previously on Mars (Maurice et al., 2022). Indeed, the former study (using only data up to $L_s = 104°$) did not consider the variation of acoustic impedance, nor the turbulence scattering. In addition, the echoes were not filtered out of the time series. Therefore, for some frequency bands, not only the energy of the direct arrival may have been integrated, which explains the observed bias between their points, this study and the model. The high frequency points (> 7 kHz) tend to match for the models computed at $L_s = 0, 70$ and $270°$ (i.e., from Northern winter to spring). Indeed, these two seasons include most of our dataset (see Fig. 3a) and it explains why the attenuation is dominated by these atmospheric conditions. The points at 3 and 5 kHz tend to be close to the model computed at $L_s = 150°$. This could be because the Gaussian pulse we used to fit the data does not perfectly represent the direct signal, or because the lower frequencies are more affected by electromagnetic contamination of the time series. Furthermore, owing to the Ingenuity data, the current study measures for the first time the attenuation at 84 Hz and 168 Hz, at a frequency where vibrational relaxation dominates the attenuation budget. However, down to the infrasound domain in the Bass and Chambers (2001) model, the attenuation evolves as a function of the frequency squared, but the height of this slope depends on parameters (e.g., relaxation frequency and relaxation strength) that are more difficult to model (Bass et al., 1984).

Here the 84 Hz point verifies the approximations used in Bass and Chambers (2001). However, in this model, only the v_2 degenerate bending vibrational mode for CO_2 is considered as it represents more than 96% of the vibrational specific heat. In contrary, first principle models that include all vibrational modes add more attenuation below ~5 Hz (see Fig. 1b in Petculescu and Lueptow (2007)). Therefore, the data presented here validate the absorption model in the high frequency part of the infrasound domain, down to ~5 Hz.

4. Conclusions and perspectives

The SuperCam microphone, combined with two temporally, spatially, and frequency-defined sound sources, the laser-induced shock waves and the Ingenuity flights, enables an active acoustic sensing of the atmosphere of Mars with which we can refine our understanding on sound propagation in the CO_2-dominated low-pressure atmosphere of Mars.

Atmospheric turbulence is identified to account for much of the variability of the laser-induced acoustic signal amplitudes: caustics are assumed to explain the high and low amplitudes peaks over a sequence of recorded waves and the overall scattering as a function of the local time is consistent with the daytime evolution of the air temperature fluctuations, which is known to be indicative of convective instabilities. Hence, this suggests that, when the goal of the microphone observation is to record small relative variations of sound amplitude within a burst of shots (e.g., to measure rock hardness or to detect surface coatings), the observation window should be scheduled during times of weak turbulence (e.g.,
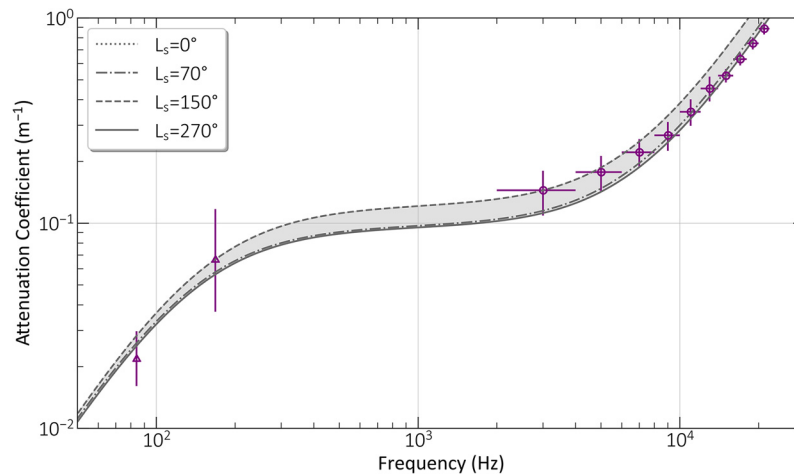
Fig. 5. Attenuation coefficient retrieved from the helicopter at low frequency (triangles), and LIBS acoustic data at high frequency (circles). For both techniques, vertical error bars are computed as the confidence interval at 95% of the fit. For the LIBS points, vertical bars also include the uncertainty on the irradiance law (see Section 2.1 and Supporting Figure S1) Horizontal error bars for the LIBS points are given as width of each frequency range considered. They are compared to the Bass and Chambers model, computed for the pressure and temperature values for $L_s = 0, 70, 150$ and $260°$ (gray lines). Lines for $L_s = 0°$ and $L_s = 270°$ are not distinguishable. All experimental points match the model within error bars, except two points at high frequency (8.8 and 21 kHz, see text).

dusk or after dawn). Furthermore, it was also noticed that the amplitude scattering increases with the propagation distance. Going further, the acoustic theory of spherical wave propagation through a turbulent medium (Iooss et al., 2000) established that this amplitude scattering, often called scintillation by analogy with optical propagation, combined with statistics on travel time with distance, helps to constrain the characteristic scale of atmospheric turbulence. Such an estimation would help to understand the apparent contradiction between the Kolmogorov theory and the in situ measurements of the turbulent pressure spectra (Banfield et al., 2020). Overall, it has been demonstrated that acoustic measurements on Mars give access to a high frequency motions within the atmosphere that are not accessible by traditional weather station such as MEDA (Maurice et al., 2022; Chide et al., 2022). This will be the focus of a future study.

Secondly, it was also observed that the sound intensity of the laser sparks varies by a factor ~1.8 over a Martian year for a given distance and for the average rock properties. We have demonstrated that the seasonal cycle of pressure and temperature on Mars is responsible for a change of the Rankine-Hugoniot conditions at the shock-wave formation and a change of the acoustic impedance for the coupling through the microphone membrane with time. Therefore, we propose an atmospheric correction that will be important to apply before any interpretation of sound amplitudes, such as to study the influence of laser-to-target coupling influence on the acoustic signal.

Finally, the evolution of both Ingenuity tones and laser sparks with distance provides *in situ* measurements of the absorption models in CO_2, at 84 Hz and 168 Hz and from 2 kHz to 20 kHz, respectively. For these frequencies, we have found that the attenuation coefficients retrieved on Mars match the existing model developed by Bass and Chambers (2001). This represents a ground truth value for this absorption model, which is key in numerical simulations used to constrain the source and location of infrasounds recorded on Mars (Martire et al., 2020; Garcia et al., 2022), but also for geophysical applications in other CO_2-rich atmospheres such as that of Venus.

Overall, given the success of the Perseverance acoustic measurements on Mars (Maurice et al., 2022; Chide et al., 2022; Murdoch et al., 2022; Stott et al., 2023; Lorenz et al., 2023), and the very low resource demands of a simple microphone, future missions may also perform acoustic studies, not only on Mars but also on other planetary atmospheres. Indeed, the Dragonfly rotorcraft mis-

sion to Titan is planned to carry one or more microphones and there are projects to study infrasounds from balloon-based platforms on Venus (Krishnamoorthy and Bowman, 2023). The results presented here show how the propagation of artificial sounds can be used to examine planetary environments (e.g. turbulence) and they show what are the key atmospheric factors (e.g. impedance, absorption) that are influencing the sound amplitude of a given source. Therefore, they will be helpful in the design of future planetary acoustic-based experiments.

CRediT authorship contribution statement

Baptiste Chide: Conceptualization, Data curation, Formal analysis, Investigation, Methodology, Visualization, Writing – original draft, Writing – review & editing. **Xavier Jacob:** Conceptualization, Methodology, Validation, Writing – original draft, Writing – review & editing. **Andi Petculescu:** Formal analysis, Methodology, Validation, Writing – original draft, Writing – review & editing. **Ralph D. Lorenz:** Formal analysis, Methodology, Validation, Writing – original draft, Writing – review & editing. **Sylvestre Maurice:** Conceptualization, Formal analysis, Resources, Supervision, Validation, Writing – original draft, Writing – review & editing. **Fabian Seel:** Formal analysis, Validation, Writing – review & editing. **Susanne Schröder:** Formal analysis, Validation, Writing – review & editing. **Roger C. Wiens:** Resources, Supervision, Validation, Writing – review & editing. **Martin Gillier:** Formal analysis, Validation, Writing – review & editing. **Naomi Murdoch:** Formal analysis, Validation, Writing – review & editing. **Nina L. Lanza:** Supervision, Validation. **Tanguy Bertrand:** Investigation, Validation, Writing – review & editing. **Timothy G. Leighton:** Investigation, Validation. **Phillip Joseph:** Investigation, Validation. **Paolo Pilleri:** Data curation, Investigation, Resources, Software, Writing – review & editing. **David Mimoun:** Investigation, Resources. **Alexander Stott:** Investigation, Validation, Writing – review & editing. **Manuel de la Torre Juarez:** Investigation, Validation. **Ricardo Hueso:** Formal analysis, Validation, Writing – review & editing. **Asier Munguira:** Formal analysis, Writing – review & editing. **Agustin Sánchez-Lavega:** Formal analysis, Validation, Writing – review & editing. **German Martinez:** Formal analysis, Validation, Writing – review & editing. **Carène Larmat:** Investigation, Validation. **Jérémie Lasue:** Investigation, Validation, Writing – review & editing. **Claire Newman:** Investigation, Validation. **Jorge Pla-Garcia:** Investigation, Validation. **Pernelle Bernardi:** Investigation, Resources. **Ari-Matti Harri:** Investigation, Resources.

Maria Genzer: Investigation, Resources. **Alain Lepinette:** Investigation, Resources.

Declaration of competing interest

The authors declare that they have no known competing financial interests or personal relationships that could have appeared to influence the work reported in this paper.

Data availability

All Perseverance data used in this study are publicly available via the Planetary Data System.

Appendix A. Supplementary material

Supplementary material related to this article can be found online at https://doi.org/10.1016/j.epsl.2023.118200.

References

Arrowsmith, S., Averbuch, G., Giannone, M.R., Sabatini, R., 2022. The use of infrasound from repeating explosion sequences in Oklahoma to probe the atmosphere. J. Acoust. Soc. Am. 151, A159. https://doi.org/10.1121/10.0010968.

Attenborough, K., 2002. Sound propagation close to the ground. Annu. Rev. Fluid Mech. 34, 51–82.

Averiyanov, M., Ollivier, S., Khokhlova, V., Blanc-Benon, P., 2011. Random focusing of nonlinear acoustic N-waves in fully developed turbulence: laboratory scale experiment. J. Acoust. Soc. Am. 130, 3595–3607. https://doi.org/10.1121/1.3652869.

Balaram, J., Aung, M., Golombek, M.P., 2021. The ingenuity helicopter on the perseverance rover. Space Sci. Rev. 217. https://doi.org/10.1007/s11214-021-00815-w.

Banfield, D., Spiga, A., Newman, C., Forget, F., Lemmon, M., Lorenz, R., Murdoch, N., Viudez-Moreiras, D., Pla-Garcia, J., Garcia, R.F., Lognonné, P., Karatekin, O., Perrin, C., Martire, L., Teanby, N., Hove, B.V., Maki, J.N., Kenda, B., Mueller, N.T., Rodriguez, S., Kawamura, T., McClean, J.B., Stott, A.E., Charalambous, C., Millour, E., Johnson, C.L., Mittelholz, A., Määttänen, A., Lewis, S.R., Clinton, J., Stähler, S.C., Ceylan, S., Giardini, D., Warren, T., Pike, W.T., Daubar, I., Golombek, M., Rolland, L., Widmer-Schnidrig, R., Mimoun, D., Beucler, E., Jacob, A., Lucas, A., Baker, M., Ansan, V., Hurst, K., Mora-Sotomayor, L., Navarro, S., Torres, J., Lepinette, A., Molina, A., Marin-Jimenez, M., Gomez-Elvira, J., Peinado, V., Rodriguez-Manfredi, J.-A., Carcich, B.T., Sackett, S., Russell, C.T., Spohn, T., Smrekar, S.E., Banerdt, W.B., 2020. The atmosphere of Mars as observed by InSight. Nat. Geosci. 13 (3), 190–198. https://doi.org/10.1038/s41561-020-0534-0.

Bass, H., Sutherland, L., Piercy, J., Evans, L., 1984. Absorption of sound by the atmosphere. In: Physical Acoustics: Principles and Methods, vol. 17, pp. 145–232.

Bass, H.E., Chambers, J.P., 2001. Absorption of sound in the Martian atmosphere. J. Acoust. Soc. Am. 109, 3069–3071. https://doi.org/10.1121/1.1365424.

Blanc-Benon, P., Juve, D., 1993. Intensity fluctuations of spherical acoustic waves propagating through thermal turbulence. Waves Random Media 3, 71–83. https://doi.org/10.1088/0959-7174/3/2/002.

Blanc-Benon, P., Juve, D., Comte-Bellot, G., 1991. Occurrence of caustics for high-frequency acoustic waves propagating through turbulent fields. Theor. Comput. Fluid Dyn. 2, 271–278. https://doi.org/10.1007/bf00271467.

Campanella, B., Legnaioli, S., Pagnotta, S., Poggialini, F., Palleschi, V., 2019. Shock waves in laser-induced plasmas. Atoms 7, 57. https://doi.org/10.3390/atoms7020057.

Chatain, A., Spiga, A., Banfield, D., Forget, F., Murdoch, N., 2021. Seasonal variability of the daytime and nighttime atmospheric turbulence experienced by InSight on Mars. Geophys. Res. Lett., 48. https://doi.org/10.1029/2021GL095453. e2021GL095453.

Chide, B., Maurice, S., Murdoch, N., Lasue, J., Bousquet, B., Jacob, X., Cousin, A., Forni, O., Gasnault, O., Meslin, P.-Y., Fronton, J.-F., Bassas-Portus, M., Cadu, A., Sournac, A., Mimoun, D., Wiens, R.C., 2019. Listening to laser sparks: a link between laser-induced breakdown spectroscopy, acoustic measurements and crater morphology. Spectrochim. Acta, Part B, At. Spectrosc. 153, 50–60. https://doi.org/10.1016/j.sab.2019.01.008.

Chide, B., Maurice, S., Cousin, A., Bousquet, B., Mimoun, D., Beyssac, O., Meslin, P.-Y., Wiens, R.C., 2020. Recording laser-induced sparks on Mars with the SuperCam microphone. Spectrochim. Acta, Part B, At. Spectrosc. 174, 106000. https://doi.org/10.1016/j.sab.2020.106000.

Chide, B., Beyssac, O., Gauthier, M., Benzerara, K., Estève, I., Boulliard, J.-C., Maurice, S., Wiens, R.C., 2021. Acoustic monitoring of laser-induced phase transitions in minerals: implication for Mars exploration with SuperCam. Sci. Rep. 11, 24019. https://doi.org/10.1038/s41598-021-03315-7.

Chide, B., Bertrand, T., Lorenz, R.D., Munguira, A., Hueso, R., Sanchez-Lavega, A., Martinez, G., Spiga, A., Jacob, X., de la Torre Juarez, M., Lemmon, M.T., Banfield, D., Newman, C.E., Murdoch, N., Stott, A., Viudez-Moreiras, D., Pla-Garcia, J., Larmat, C., Lanza, N.L., Rodriguez-Manfredi, J.A., Wiens, R.C., 2022. Acoustics reveals short-term air temperature fluctuations near Mars' surface. Geophys. Res. Lett. 49. https://doi.org/10.1029/2022gl100333.

Dalmont, J.-P., 2001. Acoustic impedance measurements, part I: a review. J. Sound Vib. 243, 427–439. https://doi.org/10.1006/jsvi.2000.3428.

De la Torre-Juarez, M., et al., 2023. Diurnal cycle of rapid air temperature fluctuations at Jezero crater: probability distributions, exponential tails, scaling, and intermittency. J. Geophys. Res., Planets. submitted for publication.

Garcia, R.F., Daubar, I.J., Beucler, E., Posiolova, L.V., Collins, G.S., Lognonne, P., Rolland, L., Xu, Z., Wojcicka, N., Spiga, A., Fernando, B., Speth, G., Martire, L., Rajsvic, A., Miljkovic, K., Sansom, E.K., Charalambous, C., Ceylan, S., Menina, S., Margerin, L., Lapeyre, R., Neidhart, T., Teanby, N.A., Schmerr, N.C., Bonnin, M., Froment, M., Clinton, J.F., Karatekin, O., Stahler, S.C., Dahmen, N.L., Duran, C., Horleston, A., Kawamura, T., Plasman, M., Zenhausern, G., Giardini, D., Panning, M., Malin, M., Banerdt, W.B., 2022. Newly formed craters on Mars located using seismic and acoustic wave data from InSight. Nat. Geosci. 15, 774–780. https://doi.org/10.1038/s41561-022-01014-0.

Grip, H.F., Conway, D., Lam, J., Williams, N., Golombek, M.P., Brockers, R., Mischna, M., Cacan, M.R., 2022. Flying a helicopter on Mars: how ingenuity's flights were planned, executed, and analyzed. In: 2022 IEEE Aerospace Conference. Big Sky, Montana.

Iooss, B., Blanc-Benon, P., Lhuillier, C., 2000. Statistical moments of travel times at second order in isotropic and anisotropic random media. Waves Random Media 10, 381–394. https://doi.org/10.1088/0959-7174/10/3/305.

Krishnamoorthy, S., Bowman, D.C., 2023. A "Floatilla" of airborne seismometers for Venus. Geophys. Res. Lett. 50 (2). https://doi.org/10.1029/2022GL100978.

Lanza, N.L., Chide, B., Clegg, S., Dauson, E., Forni, O., Larmat, C., Ollila, A., Reyes-Newell, A., Ten Cate, J., Wiens, R., Maurice, S., 2020. Listening for rock coatings on Mars: using acoustic signals from laser-induced breakdown spectroscopy to identify surface coating and layers. In: 51st Lunar and Planetary Science Conference. The Woodlands, TX, United States, p. 2807.

Lemmon, M.T., Lorenz, R.D., Rabinovitch, J., Newman, C.E., Williams, N.R., Sullivan, R., Golombek, M.P., Bell III, J.F., Maki, J.N., Vicente-Retortillo, A., 2022. Lifting and transport of Martian dust by the ingenuity helicopter rotor downwash as observed by high-speed imaging from the perseverance rover. J. Geophys. Res., Planets. https://doi.org/10.1029/2022je007605.

Lorenz, R.D., Maurice, S., Chide, B., Mimoun, D., Stott, A.E., Murdoch, N., Gillier, M., Jacob, X., Wiens, R.C., Montmessin, F., Grip, H., Tzanetos, T., Balaram, B., Williams, N., Keennon, M., Langberg, S., Tyler, J., Bertrand, T., Brown, A., Randazzo, N., Pipenberg, B., 2023. The sound of a helicopter on Mars. Planet. Space Sci. https://doi.org/10.1016/j.pss.2023.105684.

Martinez, G.M., Sebastiian, E., Vicente-Retortillo, A., Smith, M.D., Johnson, J.R., Fischer, E., Savijarvi, H., Toledo, D., Hueso, R., Mora-Sotomayor, L., Gillespie, H., Munguira, A., Sanchez-Lavega, A., Lemmon, M.T., Gomez, F., Polkko, J., Mandon, L., Apestigue, V., Arruego, I., Ramos, M., Conrad, P., Newman, C.E., de la Torre-Juarez, M., Jordan, F., Tamppari, L.K., McConnochie, T.H., Harri, A.-M., Genzer, M., Hieta, M., Zorzano, M.-P., Siegler, M., Prieto, O., Molina, A., Rodriguez-Manfredi, J.A., 2023. Surface energy budget, albedo and thermal inertia at Jezero crater, Mars, as observed from the Mars 2020 MEDA instrument. J. Geophys. Res., Planets. https://doi.org/10.1029/2022je007537.

Martire, L., Garcia, R.F., Rolland, L., Spiga, A., Lognonne, P.H., Banfield, D., Banerdt, W.B., Martin, R., 2020. Martian infrasound: numerical modeling and analysis of InSight's data. J. Geophys. Res., Planets 125. https://doi.org/10.1029/2020je006376.

Maurice, S., Wiens, R.C., Bernardi, P., Cais, P., Robinson, S., Nelson, T., Gasnault, O., Reess, J.-M., Deleuze, M., Rull, F., Manrique, J.-A., Abbaki, S., Anderson, R.B., Andre, Y., Angel, S.M., Arana, G., Battault, T., Beck, P., Benzerara, K., Bernard, S., Berthias, J.-P., Beyssac, O., Bonafous, M., Bousquet, B., Boutillier, M., Cadu, A., Castro, K., Chapron, F., Chide, B., Clark, K., Clave, E., Clegg, S., Cloutis, E., Collin,

C., Cordoba, E.C., Cousin, A., Dameury, J.-C., D'Anna, W., Daydou, Y., Debus, A., Deflores, L., Dehouck, E., Delapp, D., Santos, G.D.L., Donny, C., Doressoundiram, A., Dromart, G., Dubois, B., Dufour, A., Dupieux, M., Egan, M., Ervin, J., Fabre, C., Fau, A., Fischer, W., Forni, O., Fouchet, T., Frydenvang, J., Gauffre, S., Gauthier, M., Gharakanian, V., Gilard, O., Gontijo, I., Gonzalez, R., Granena, D., Grotzinger, J., Hassen-Khodja, R., Heim, M., Hello, Y., Hervet, G., Humeau, O., Jacob, X., Jacquinod, S., Johnson, J.R., Kouach, D., Lacombe, G., Lanza, N., Lapauw, L., Laserna, J., Lasue, J., Deit, L.L., Mouelic, S.L., Comte, E.L., Lee, Q.-M., Legett, C., Leveille, R., Lewin, E., Leyrat, C., Lopez-Reyes, G., Lorenz, R., Lucero, B., Madariaga, J.M., Madsen, S., Madsen, M., Mangold, N., Manni, F., Mariscal, J.-F., Martinez-Frias, J., Mathieu, K., Mathon, R., McCabe, K.P., McConnochie, T., McLennan, S.M., Mekki, K., Melikechi, N., Meslin, P.-Y., Micheau, Y., Michel, Y., Michel, J.M., Mimoun, D., Misra, A., Montagnac, G., Montaron, C., Montmessin, F., Moros, J., Mousset, V., Morizet, Y., Murdoch, N., Newell, R.T., Newsom, H., Tuong, N.N., Ollila, A.M., Orttner, G., Oudda, L., Pares, L., Parisot, J., Parot, Y., Perez, R., Pheav, D., Picot, L., Pilleri, P., Pilorget, C., Pinet, P., Pont, G., Poulet, F., Quantin-Nataf, C., Quertier, B., Rambaud, D., Rapin, W., Romano, P., Roucayrol, L., Royer, C., Ruellan, M., Sandoval, B.F., Sautter, V., Schoppers, M.J., Schroder, S., Seran, H.-C., Sharma, S.K., Sobron, P., Sodki, M., Sournac, A., Sridhar, V., Standarovsky, D., Storms, S., Striebig, N., Tatat, M., Toplis, M., Torre-Fdez, I., Toulemont, N., Velasco, C., Veneranda, M., Venhaus, D., Virmontois, C., Viso, M., Willis, P., Wong, K.W., 2021. The SuperCam instrument suite on the Mars 2020 rover: science objectives and mast-unit description. Space Sci. Rev. 217. https://doi.org/10.1007/s11214-021-00807-w.

Maurice, S., Chide, B., Murdoch, N., Lorenz, R.D., Mimoun, D., Wiens, R.C., Stott, A., Jacob, X., Bertrand, T., Montmessin, F., Lanza, N.L., Alvarez-Llamas, C., Angel, S.M., Aung, M., Balaram, J., Beyssac, O., Cousin, A., Delory, G., Forni, O., Fouchet, T., Gasnault, O., Grip, H., Hecht, M., Hoffman, J., Laserna, J., Lasue, J., Maki, J., Mc-Clean, J., Meslin, P.-Y., Mouelic, S.L., Munguira, A., Newman, C.E., Manfredi, J.A.R., Moros, J., Ollila, A., Pilleri, P., Schroder, S., de la Torre Juarez, M., Tzanetos, T., Stack, K.M., Farley, K., Williford, K., The SuperCam team, 2022. In situ recording of Mars soundscape. Nature 605, 653–658. https://doi.org/10.1038/s41586-022-04679-0.

Mimoun, D., Cadu, A., Murdoch, N., Chide, B., Sournac, A., Parot, Y., Bernardi, P., Pilleri, P., Stott, A., Gillier, M., Sridhar, V., Maurice, S., Wiens, R.C., The SuperCam team, 2023. The Mars microphone onboard SuperCam. Space Sci. Rev. 219, 5. https://doi.org/10.1007/s11214-022-00945-9.

Munguira, A., Hueso, R., Sanchez-Lavega, A., de la Torre-Juarez, M., Martinez, G., Newman, C.E., Sebastian, E., Lepinette, A., Vicente-Retortillo, A., Chide, B., Lemmon, M.T., Bertrand, T., Lorenz, R., Banfield, D., Gomez-Elvira, J., Martin-Soler, J., Navarro, S., Pla-Garcia, J., Rodriguez-Manfredi, J.A., Romeral, J., Smith, M.D., Torres, J., 2023. Near surface atmospheric temperatures at Jezero from Mars 2020 MEDA measurements. J. Geophys. Res., Planets. https://doi.org/10.1029/2022je007559.

Murdoch, N., Chide, B., Lasue, J., Cadu, A., Sournac, A., Bassas-Portus, M., Jacob, X., Merrison, J., Iversen, J., Moretto, C., Velasco, C., Pares, L., Hynes, A., Godiver, V., Lorenz, R., Cais, P., Bernadi, P., Maurice, S., Wiens, R., Mimoun, D., 2019. Laser-induced breakdown spectroscopy acoustic testing of the Mars 2020 microphone. Planet. Space Sci. 165, 260–271. https://doi.org/10.1016/j.pss.2018.09.009.

Murdoch, N., Stott, A.E., Gillier, M., Hueso, R., Lemmon, M., Martinez, G., Apestigue, V., Toledo, D., Lorenz, R.D., Chide, B., Munguira, A., Sanchez-Lavega, A., Vicente-Retortillo, A., Newman, C.E., Maurice, S., de la Torre Juarez, M., Bertrand, T., Banfield, D., Navarro, S., Marin, M., Torres, J., Gomez-Elvira, J., Jacob, X., Cadu, A., Sournac, A., Rodriguez-Manfredi, J.A., Wiens, R.C., Mimoun, D., 2022. The sound of a Martian dust devil. Nat. Commun. 13 (1). https://doi.org/10.1038/s41467-022-35100-z.

Petculescu, A., Lueptow, R.M., 2007. Atmospheric acoustics of Titan, Mars, Venus, and Earth. Icarus 186, 413–419. https://doi.org/10.1016/j.icarus.2006.09.014.

Petrosyan, A., Galperin, B., Larsen, S.E., Lewis, S.R., Maattanen, A., Read, P.L., Renno, N., Rogberg, L.P.H.T., Savijarvi, H., Siili, T., Spiga, A., Toigo, A., Vazquez, L., 2011. The Martian atmospheric boundary layer. Rev. Geophys. 49. https://doi.org/10.1029/2010rg000351.

Rodriguez-Manfredi, J.A., de la Torre Juarez, M., Alonso, A., Apestigue, V., Arruego, I., Atienza, T., Banfield, D., Boland, J., Carrera, M.A., Castaner, L., Ceballos, J., Chen-Chen, H., Cobos, A., Conrad, P.G., Cordoba, E., del Rio-Gaztelurrutia, T., de Vicente-Retortillo, A., Dominguez-Pumar, M., Espejo, S., Fairen, A.G., Ferniandez-Palma, A., Ferrandiz, R., Ferri, F., Fischer, E., Garcia-Manchado, A., Garcia-Villadangos, M., Genzer, M., Gimenez, S., Gomez-Elvira, J., Gomez, F., Guzewich, S.D., Harri, A.-M., Hernandez, C.D., Hieta, M., Hueso, R., Jaakonaho, I., Jimenez, J.J., Jimenez, V., Larman, A., Leiter, R., Lepinette, A., Lemmon, M.T., Lopez, G., Madsen, S.N., Makinen, T., Marin, M., Martin-Soler, J., Martinez, G., Molina, A., Mora-Sotomayor, L., Moreno-Alvarez, J.F., Navarro, S., Newman, C.E., Ortega, C., Parrondo, M.C., Peinado, V., Pena, A., Perez-Grande, I., Perez-Hoyos, S., Pla-Garcia, J., Polkko, J., Postigo, M., Prieto-Ballesteros, O., Rafkin, S.C.R., Ramos, M., Richardson, M.I., Romeral, J., Romero, C., Runyon, K.D., Saiz-Lopez, A., Sanchez-Lavega, A., Sard, I., Schofield, J.T., Sebastian, E., Smith, M.D., Sullivan, R.J., Tamppari, L.K., Thompson, A.D., Toledo, D., Torrero, F., Torres, J., Urqui, R., Velasco, T., Viudez-Moreiras, D., Zurita, S., 2021. The Mars environmental dynamics analyzer, MEDA. A suite of environmental sensors for the Mars 2020 mission. Space Sci. Rev. 217. https://doi.org/10.1007/s11214-021-00816-9.

Salze, E., Yuldashev, P., Ollivier, S., Khokhlova, V., Blanc-Benon, P., 2014. Laboratory-scale experiment to study nonlinear N-wave distortion by thermal turbulence. J. Acoust. Soc. Am. 136, 556–566. https://doi.org/10.1121/1.4887458.

Sanchez-Lavega, A., del Rio-Gaztelurrutia, T., Hueso, R., de la Torre Juarez, M., Martinez, G.M., Harri, A.-M., Genzer, M., Hieta, M., Polkko, J., Rodriguez-Manfredi, J.A., Lemmon, M.T., Pla-Garcia, J., Toledo, D., Vicente-Retortillo, A., Viudez-Moreiras, D., Munguira, A., Tamppari, L.K., Newman, C., Gomez-Elvira, J., Guzewich, S., Bertrand, T., Apestigue, V., Arruego, I., Wolff, M., Banfield, D., Jaakonaho, I., Makinen, T., 2023. Mars 2020 perseverance rover studies of the Martian atmosphere over Jezero from pressure measurements. J. Geophys. Res., Planets 128. https://doi.org/10.1029/2022je007480.

Seel, F., Schroder, S., Vogt, D., Dietz, E., Hubers, H.-W., Gensch, M., 2023. Generation and evolution of laser-induced shock waves under Martian atmospheric conditions. Icarus 394, 115405. https://doi.org/10.1016/j.icarus.2022.115405.

Stott, A.E., Murdoch, N., Gillier, M., Banfield, D., Bertrand, T., Chide, B., de la Torre Juarez, M., Hueso, R., Lorenz, R., Martinez, G., Munguira, A., Mora Sotomayor, L., Navarro, S., Newman, C., Pilleri, P., Pla-Garcia, J., Rodriguez-Manfredi, J.-A., Sanchez-Lavega, A., Smith, M., Viudez Moreiras, D., Williams, N., Maurice, S., Wiens, R.C., Mimoun, D., 2023. Wind and turbulence observations with the Mars microphone on Perseverance. J. Geophys. Res., Planets. https://doi.org/10.1029/2022JE007547.

Taylor, G., 1950. The formation of a blast wave by a very intense explosion I. Theoretical discussion. Proc. R. Soc. Lond. Ser. A, Math. Phys. Sci. 201, 159–174. https://doi.org/10.1098/rspa.1950.0049.

Thom, H.C.S., 1958. A note on the gamma distribution. Mon. Weather Rev. 86, 117–122. https://doi.org/10.1175/1520-0493(1958)086<0117:anotgd>2.0.co;2.

Trainer, M.G., Wong, M.H., McConnochie, T.H., Franz, H.B., Atreya, S.K., Conrad, P.G., Lefevre, F., Mahaffy, P.R., Malespin, C.A., Manning, H.L., Martin-Torres, J., Martinez, G.M., McKay, C.P., Navarro-Gonzalez, R., Vicente-Retortillo, A., Webster, C.R., Zorzano, M.-P., 2019. Seasonal variations in atmospheric composition as measured in Gale crater, Mars. J. Geophys. Res., Planets. https://doi.org/10.1029/2019je006175.

Wiens, R.C., Maurice, S., Robinson, S.H., Nelson, A.E., Cais, P., Bernardi, P., Newell, R.T., Clegg, S., Sharma, S.K., Storms, S., Deming, J., Beckman, D., Ollila, A.M., Gasnault, O., Anderson, R.B., Andre, Y., Angel, S.M., Arana, G., Auden, E., Beck, P., Becker, K., Benzerara, K., Bernard, S., Beyssac, O., Borges, L., Bousquet, B., Boyd, K., Carey, M., Carlson, J., Castro, K., Celis, J., Chide, B., Clark, K., Cloutis, E., Cordoba, E.C., Cousin, A., Dale, M., Deflores, L., Delapp, D., Deleuze, M., Dirmyer, M., Donny, C., Dromart, G., Duran, M.G., Egan, M., Ervin, J., Fabre, C., Fau, A., Fischer, W., Forni, O., Fouchet, T., Fresquez, R., Frydenvang, J., Gasway, D., Gontijo, I., Grotzinger, J., Jacob, X., Jacquinod, S., Johnson, J.R., Klisiewicz, R.A., Lake, J., Lanza, N., Laserna, J., Lasue, J., Mouelic, S.L., Legett, C., Leveille, R., Lewin, E., Lopez-Reyes, G., Lorenz, R., Lorigny, E., Love, S.P., Lucero, B., Madariaga, J.M., Madsen, M., Madsen, S., Mangold, N., Manrique, J.A., Martinez, J.P., Martinez-Frias, J., McCabe, K.P., McConnochie, T.H., McGlown, J.M., McLennan, S.M., Melikechi, N., Meslin, P.-Y., Michel, J.M., Mimoun, D., Misra, A., Montagnac, G., Montmessin, F., Mousset, V., Murdoch, N., Newsom, H., Ott, L.A., Ousnamer, Z.R., Pares, L., Parot, Y., Pawluczyk, R., Peterson, C.G., Pilleri, P., Pinet, P., Pont, G., Poulet, F., Provost, C., Quertier, B., Quinn, H., Rapin, W., Reess, J.-M., Regan, A.H., Reyes-Newell, A.L., Romano, P.J., Royer, C., Rull, F., Sandoval, B., Sarrao, J.H., Sautter, V., Schoppers, M.J., Schroder, S., Seitz, D., Shepherd, T., Sobron, P., Dubois, B., Sridhar, V., Toplis, M.J., Torre-Fdez, I., Trettel, I.A., Underwood, M., Valdez, A., Valdez, J., Venhaus, D., Willis, P., 2020. The SuperCam instrument suite on the NASA Mars 2020 rover: body unit and combined system tests. Space Sci. Rev. 217. https://doi.org/10.1007/s11214-020-00777-5.

Williams, J.-P., 2001. Acoustic environment of the Martian surface. J. Geophys. Res., Planets 106, 5033–5041. https://doi.org/10.1029/1999je001174.

Zel'dovich, Y., Raizer, Y., 1967. Physics of Shock Waves and High-Temperature Hydrodynamic Phenomena. Elsevier.